ORIGINAL RESEARCH ARTICLE

Effect of Laser Powder Bed Fusion Process Parameters on Structural, Mechanical, and Tribological Properties of AlSi7Mg Alloy

FURKAN CENGIZ, TEVFIK OĞUZHAN ERGÜDER, and FATIH YILDIZ

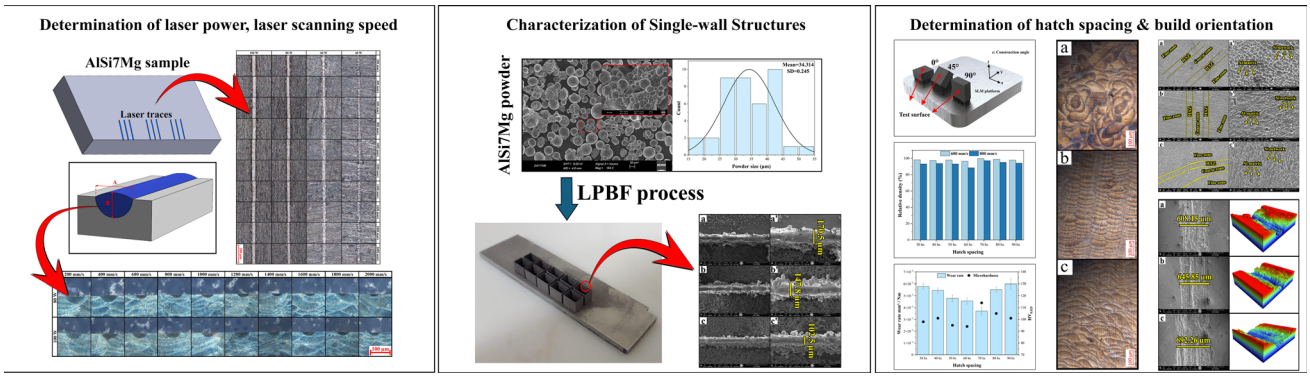

https://doi.org/10.1007/s11663-025-03867-3
© The Minerals, Metals & Materials Society and ASM International 2025

I. INTRODUCTION

BECAUSE of their exceptional strength-to-weight ratio, exceptional resistance to corrosion, and advantageous weldability, aluminum–silicon alloys show a wide range of potential applications in the aerospace, automotive, and traditional manufacturing sectors.[1–4] Thin-walled and complexly shaped items are challenging to prepare using most traditional production techniques. The development of innovative production techniques is crucial for the continued use of aluminum alloy.

One of the additive manufacturing (AM) techniques, laser powder bed fusion (LPBF), is an efficient method for producing intricate structures such as lattice and porous ones as well as innovative functional parts.[5–8] The production techniques and parameters have a considerable impact on the structural, mechanical, and tribological qualities of the items made using the LPBF technology.

The effect of process parameters on the microstructural and mechanical properties of AlSi7Mg alloy in additive manufacturing processes has been investigated in detail in many studies. The impact of process variables on the mechanical and microstructural characteristics of AlSi7Mg alloy was assessed by Rao *et al.*[9]. They discovered that the build orientation and processing parameters had a direct impact on the samples' mechanical qualities. The study by Yang *et al.*[10] focused on analyzing the mechanical behavior and microstructure of AlSi7Mg fabricated through the WAAM method. Nakamoto[11] examined LPBF-fabricated AlSi7Mg mechanically and microstructurally. The study discovered that optimal laser irradiation results in a fine dendritic microstructure and a relative density of 99.8 pct. Dense LPBF samples have significantly better yield strength, tensile strength, and elongation at break than cast materials (200 MPa, 400 MPa, and 12–17 pct,

FURKAN CENGIZ is with the Department of Mechanical Engineering, Erzurum Technical University, 25100 Erzurum, Turkey and also with the Department of Opticianry Program, Kilis 7 Aralik University, 79000 Kilis, Turkey. TEVFIK OĞUZHAN ERGÜER is with the Department of Mechanical Engineering, Erzurum Technical University, 25100 Erzurum, Turkey and also with the Department of Opticianry Program, Kilis 7 Aralik University, 79000 Kilis, Turkey. FATIH YILDIZ is with the Department of Mechanical Engineering, Erzurum Technical University, 25100 Erzurum, Turkey. Contact e-mail: furkan.cengiz11@erzurum.edu.tr; furkan.cengiz@kilis.edu.tr.

Manuscript submitted August 13, 2025; accepted November 3, 2025.

Article published online November 14, 2025.

in turn). The impact of process and powder factors on the density and hardness of AlSi7Mg alloy was researched by Tonelli *et al.*[12] Since spherical powders produced larger densities, they discovered that the shape of the powder had the greatest impact on component density. They also demonstrated a relationship between the cooling rate and the hardness rating. Casati and Vedani[13] studied how different heat treatment procedures affect the hardness and tensile qualities of A357 alloy. Aging can drastically affect mechanical characteristics. Therefore, the heat treatment approach must be properly devised. In their comparison of the mechanical and microstructural characteristics of the AlSi7Mg0.6 alloy as-cast and as-built, Pereira *et al.*[14] demonstrated that the LPBF-fabricated samples had superior mechanical qualities both before to and during heat treatment. With the right set of process conditions, they also demonstrated that the relative density of LPBF samples may rise to 99.96 pct. Oliveira de Menezes *et al.*[15] produced samples from AlSi7Mg through LPBF with build directions of 0 and 90 deg assessed their tensile characteristics.

A review of existing studies reveals that tribological properties of AlSi7Mg produced by LPBF have been largely overlooked, with most prior research focusing predominantly on microstructural and mechanical aspects. In typical LPBF applications, production parameters such as scanning speed, hatch spacing, layer thickness, and laser power are kept constant for a given energy density. However, the specific influence of these parameters on the combined microstructural, mechanical, and tribological behavior remains insufficiently explored. Notably, the role of hatch spacing and build orientation in determining the wear performance of AlSi7Mg within the LPBF framework has not been adequately addressed in the literature. Thus, in this work, the impacts of LPBF production parameters on the structural and mechanical and tribological properties of AlSi7Mg were examined.

II. MATERIALS AND METHODS

In this study, the AlSi7Mg powder utilized in LPBF-based production was obtained from a commercial supplier, and its chemical composition is presented in Table I.

Figure 1 depicts the morphology and size distribution of the powdered AlSi7Mg alloy produced through gas atomization. It is evident that the AlSi7Mg powder has a smooth surface and good sphericity. With an average size of 34 μm, powder particles can range in size from 15 to 55 μm.

Under various process conditions, a Concept Laser M LabR LPBF system (maximum power: 100 W) was used to fabricate the test samples for structural, mechanical, and tribological investigations. All productions were conducted in an argon atmosphere utilizing continuous laser pulse mode. Prior studies have demonstrated that insufficient melting can lead to the formation of undesirable precipitates, particularly with increasing layer thickness.[16,17] Conversely, reducing the layer size has been shown to promote the development of favorable morphological textures in the microstructure.[2] Based on these findings, a layer thickness of 15 μm was selected for the LPBF fabrication of AlSi7Mg alloy in this study to optimize microstructural integrity and minimize defects.

Throughout the production process, the oxygen concentration was controlled below 0.4 pct. AutoFab software was used to create STL file formats for manufactured test samples. To study the formation of molten pools under various conditions, single laser pulses were applied to a casted AlSi7Mg plate. Both the laser beam strength (from 20 to 100 W in 20 increments) and the laser scanning speed (from 200 to 2000 mm/s in 200 increments) were used to apply these laser pulses. To examine the cross-sectional images, the middle of the plate was cut perpendicular to the laser lines. The samples were then polished with diamond suspension after being sanded using water sandpaper bearing the numbers 400, 600, 800, and 1200, respectively. The Zeiss Axio A1 optical microscope was used to take the cross-sectional pictures. The aspect ratios ($R = A/2B$) were then computed after the depth (B) and width (A) of the melt pools were measured. The values of scanning speed and laser power that gave the R value closest to 1 were identified. After determining laser power and scanning speed in the first stage, single-wall samples of $6 \times 4 \times 5$ dimensions were manufactured on AlSi7Mg plate to determine wall thickness in the second stage. The wall thickness of the manufactured samples was measured using the Quanta FEG-250 scanning electron microscope (SEM). In this work, hatch spacing (hs) was defined as a percentile of the wall thickness (WT) to standardize its parametric evaluation. After optimizing the laser power and scanning speed, the influence of hatch spacing—the distance between adjacent melt pool centers—on relative density was investigated. Prismatic samples ($10 \times 10 \times 5$ mm) were fabricated with hatch spacing values incrementally increased from 30 to 90 pct of the calculated WT (in 10 pct intervals) to systematically assess its effects. The relative density of the fabricated samples was primarily determined using the Archimedes' principle, in accordance with ASTM B311 standards. Using a precision balance ($\pm$ 0.01 g), the mass of the sample was measured in air and

Table I. Chemical Compositions of the AlSi7Mg Alloy (Wt Pct)

Alloy Element	Si	Mg	Mn	Cu	Fe	Zn	Ni	Ti	Al	Pb	Sn
AlSi7Mg	9.82	0.29	<0.005	<0.005	0.082	0.006	<0.005	<0.005	Bal.	<0.005	<0.005

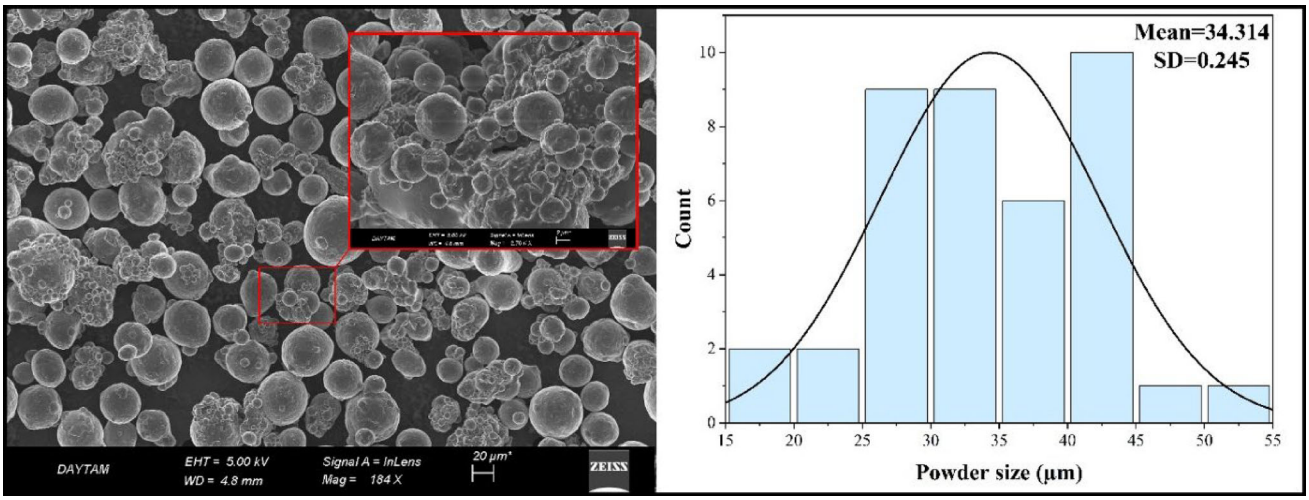

Fig. 1—SEM image and powder distribution graph of AlSi7Mg alloy powder.

subsequently in distilled water, with the density calculated from the mass difference. Each measurement was repeated three times to ensure statistical reliability. The results obtained from the Archimedes method were further verified through quantitative image analysis. For this, cross-sectional pictures taken with an optical microscope were processed using ZEISS ZEN 3.7 software, and the relative density was ascertained based on the area fraction of porosity. Following the determination of the hatch spacing value, prismatic samples were manufactured using the previously specified dimensions in the various orientations (0, 45, and 90 deg) depicted in Figure 2. to ascertain the impact of the build orientation on the density and wear characteristics.

The Bruker-Universal Mechanical Tester (Bruker-UMT) tribometer was used to test the samples for wear. The Viewer application was used to assess the data that was acquired from the experiment. Three distinct tests were conducted on various areas of the sample surface for each of the wear test parameters, which are listed in Table II. The applied load, sliding speed and duration were chosen in line with commonly reported values for LPBF produced Al–Si–Mg alloys, as demonstrated for example by Wang *et al.*[18] and Venettaci *et al.*[19] , thereby allowing both reliable assessment and direct comparison with earlier tribological investigations.

Wear traces were analyzed using a 3D profilometer following the test. The Vision program was used to process the images. By multiplying the wear traces profile area with its length, the wear volume was calculated, which was then used to determine the wear rate (mm^3/Nm). After fabrication, surface roughness was evaluated using a Bruker Contour GT 3D optical profilometer. Images of three distinct areas of the sample surface were used to measure surface roughness, and the Vision software was used to read and average the surface roughness values (R_a) on five different lines. The samples' microhardness was measured with the SHIMADZU HMV-G20 microhardness tester. In order to perform these measurements, the Vickers method was used to take minimum five measurements from various areas of the sample surface while it was subjected to a 25 g load for 10 seconds.

The GNR-Explorer XRD equipment used Cu-Ka radiation with a wavelength of k = 1.5405 A to identify the phases on the samples made using the LPBF process. In the 10–90 range, measurements were made using a

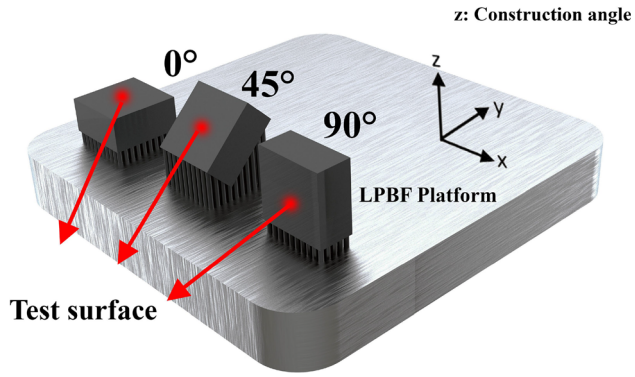

Fig. 2—Schematic illustration of prismatic samples produced using the LPBF technique in various build orientations.

Table II. Wear test parameters

Wear Test Parameters	Values
Test Type	reciprocating
Normal Load (N)	2
Stroke (mm)	4
Velocity (mm/s)	8
Counter Ball Material	Al_2O_3
Time (s)	1200
Environment	dry conditions
Temperature (°C)	room temperatures (23±2)

symmetrical scan setup at 0.05 steps per second. Using Match software, the acquired peak cards were analyzed and contrasted with findings from previous research.

To examine the microstructure of each sample, SiC paper (P400-P1200) was mechanically ground with an alumina suspension of 1 μm. After that, a Keller reagent (90 ml H_2O + 5 ml HNO_3 + 3 ml HCl + 2 ml HF) was used to etch the samples.

III. RESULTS AND DISCUSSION

A. *Surface and Melting Pool Morphology of Single-Tracks*

Single laser tracks were applied to AlSi7Mg plates to evaluate their homogeneity, which is essential for LPBF production. Figure 3 displays optical microscope morphological images of the sample top surfaces, whereas Figure 4 shows cross-sectional images of the melting pools. The generation of single laser traces was found to be significantly influenced by both scanning speed and laser power values. As the scanning speed increased for the identical laser power, it was determined that the trace widths shrank. Due to the energy density not being at the necessary power, inadequate melting was seen in laser exposures performed with low laser power. At scanning speeds ranging from 200 to 2000 mm/s and laser power of 20 W, no laser traces were seen. Also, only a surface trace was visible on the AlSi7Mg sample due to the laser exposures carried out at 40 W laser power and 200–2000 mm/s scanning speed, which could be seen on the microscope using a separate filter. Melt pools were shown to occur at 80 and 100 W power, however, cross-sectional images and a significant melting depth were not possible at other powers because to the relatively low energy input.

The proportional characteristics of the melt pool at different laser powers and scanning speeds are displayed in Table III. The shape of the melt pool is reflected in the aspect ratio (R) values. $R \geq 1$ indicates a conductive mode with an oval melt pool, while $R < 1$ indicates the keyhole mode. In manufacturing conditions with high laser power and low scanning speed values, the keyhole form typically appears. The melt pool changes from a V to an oval form when it moves from keyhole to conductive mode. Porous structures were observed in keyhole mode melt pools at late phases of manufacturing, as described in numerous research.[20] Manufacturing parameters that promote conductive mode melt pools are preferred, as they enable a more uniform heat distribution within the melt pool and consequently lead to the formation of dense, non-porous structures.[21] At 100-W laser beam power, the ideal melt pool forms were found at 400, 600, and 800 mm/s scanning speed



Fig. 3—Top surface images of single laser tracks carried out at different scanning speeds and laser powers.

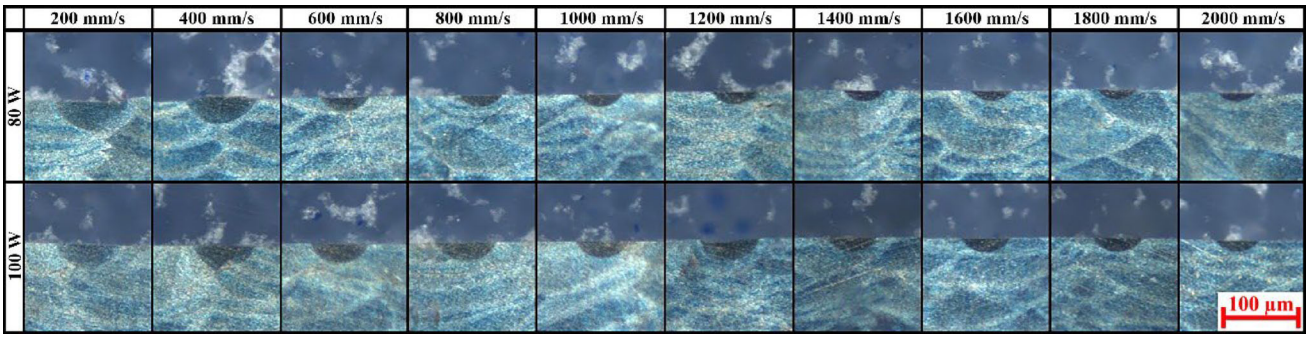

Fig. 4—Single laser tracks melt pool images at different laser powers and scanning speeds.

Table III. R Ratios and The Melt Pool's Dimensions were Measured Using Various Scanning Speeds and 80 and 100 W of Power

Laser Power (W)	Scanning Speed (mm/s)	Width—A (μm)	Depth—B (μm)	Ratio—R
80	200	86.24	28.7	1.5
	400	61.99	19.98	1.55
	600	56.12	17.06	1.64
	800	54.67	15.49	1.76
	1000	53.09	15.08	1.75
	1200	64.99	22.66	1.57
	1400	48.28	12.64	1.9
	1600	47.54	11.25	2.11
	1800	44.88	11.68	1.92
	2000	41.48	10.06	2.06
100	200	82.03	27.43	1.49
	400	79.44	27.2	1.46
	600	68.33	23.77	1.43
	800	70.47	23.66	1.48
	1000	65.26	20.73	1.57
	1200	65.79	21.46	1.56
	1400	55.98	16.97	1.64
	1600	57.3	16.44	1.74
	1800	56.24	16.69	1.68
	2000	50.8	13.78	1.84

parameters with conductive mode and aspect ratios close to 1, taking into account the aspect ratio (R) values listed in Table III.

IV. CHARACTERIZATION OF SINGLE-WALL STRUCTURES

Following the melt pool morphology analysis, the optimal laser processing parameters were identified as 400, 600, and 800 mm/s scanning speeds under a constant laser power of 100 W, which were subsequently used for single-wall fabrication. Figure 5 presents SEM micrographs of the single-wall structures employed to determine the most suitable scanning speed. At 400 mm/s [Figure 5(a)–(a')], the relatively high energy density associated with the lower scanning velocity caused excessive melting and the formation of a thick wall with a rough and irregular morphology. Pronounced material spattering and uneven edges indicated thermal instability and localized overmelting. In contrast, the wall produced at 600 mm/s [Figure 5(b)–(b')] exhibited a well-balanced energy input, leading to superior geometric uniformity and surface integrity. The measured average wall thickness was 147.8 μm, and the structure was dense, continuous, and free from major surface defects. To quantitatively assess dimensional regularity, wall thickness values were measured at five different positions on SEM cross-sections using ImageJ software. The standard deviation of these measurements was calculated as an indicator of profile uniformity. The wall fabricated at 800 mm/s exhibited the lowest thickness variation ($\pm$9.6 μm), followed by the 600 mm/s wall ($\pm$11.3 μm) and the 400 mm/s wall ($\pm$12.8 μm). Although the 800 mm/s sample showed slightly better dimensional uniformity, minor under-melting and localized discontinuities were observed at this condition. In contrast, the 600 mm/s wall demonstrated both high geometric homogeneity and stable surface morphology. Therefore, based on the combined assessment of wall uniformity and dimensional consistency, the scanning speeds of 600 mm/s and 800 mm/s were selected as the optimal parameters for subsequent sample fabrication.

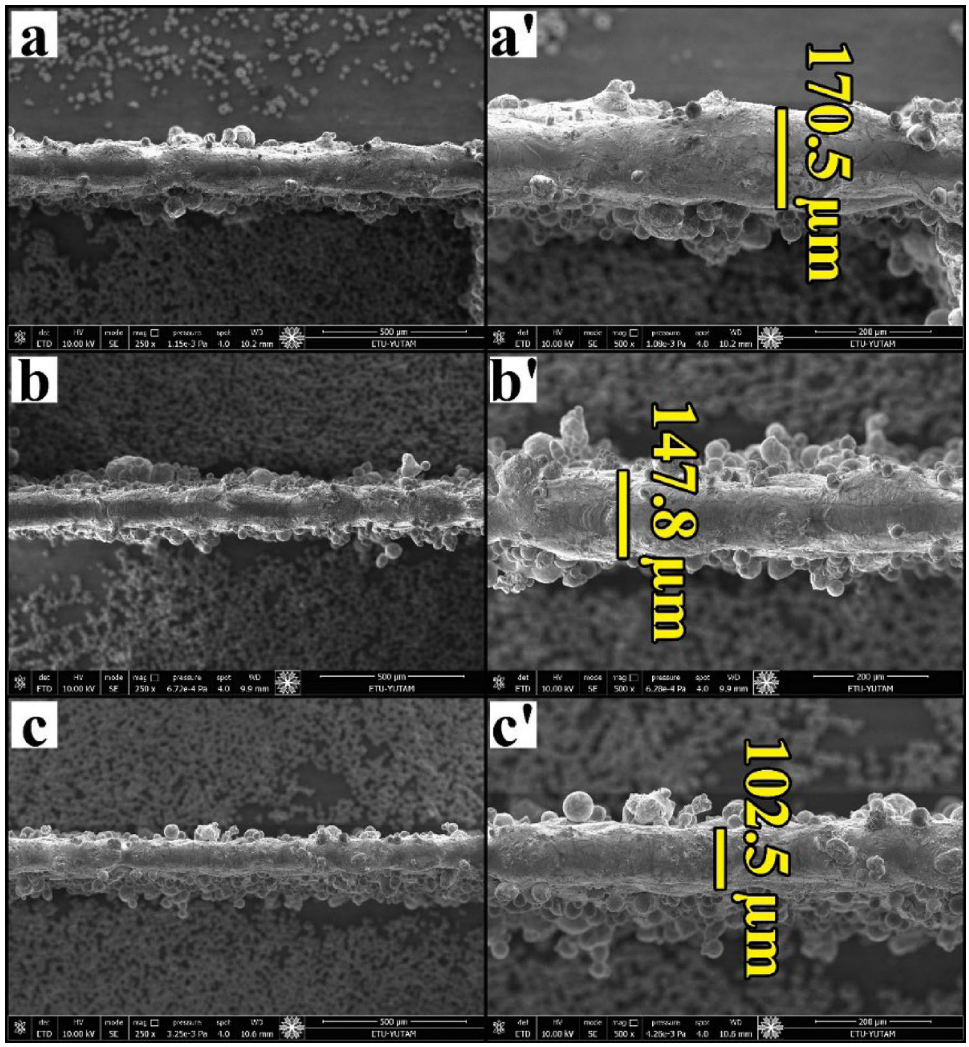

Fig. 5—SEM images of single-wall structures, (*a*)–(*a*)′ 100W-400 mm/s, (*b*)–(*b*)′ 100W-600 mm/s, (*c*)–(*c*)′ 100W-800 mm/s.

A. *Hatch Spacing Parameter Optimization*

To evaluate the effect of hatch spacing on relative density and wear behavior, prismatic samples ($10 \times 10 \times 5$ mm^3) were fabricated using varying hatch spacing values. The experiments were conducted with a fixed laser power of 100 W and scanning speeds of 600–800 mm/s. Initial trials employed hatch spacings that were incrementally increased from 30 to 90 pct (in 10 pct intervals) of the calculated wall thickness. The relative density values calculated using the Archimedes method are presented graphically in Figure 6. The relative density values of prismatic samples produced with parameters of 100–600 mm/s and 100 W–800 mm/s at different hatch spacing values, as calculated by the Archimedes method, are presented in Table IV. Upon combined evaluation of Figure 6 and Table IV, it was determined that the samples produced with a scanning speed of 600 mm/s exhibited higher relative density values compared to those produced at 800 mm/s. This result can be attributed to the higher volumetric energy density at the lower scanning speed, which promotes more complete melting of the powder and improved

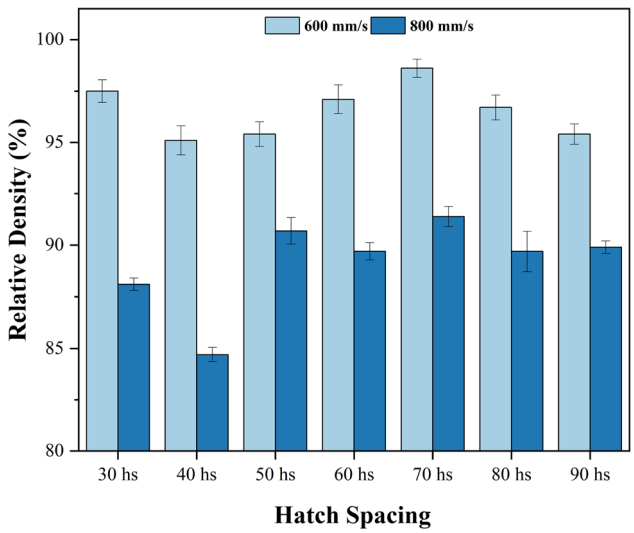

Fig. 6—Graphical distribution of relative density values determined by Archimedes' method.

overlap between adjacent scan tracks, thereby reducing porosity formation.[22,23] Furthermore, among all fabricated samples, the highest relative density value was achieved by the specimen produced with the parameter set of 600 mm/s scanning speed, and 70 pct hatch spacing.

Table IV. Values of Relative Densities Calculated by the Archimedes' Method

Hatch Spacing (Pct)	Relative Density (Pct)	
	100 W-600 mm/s	100 W-800 mm/s
30 hs	97.5 ± 0.95	88.1 ± 0.52
40 hs	97.48 ± 1.21	84.7 ± 0.6
50 hs	97.89 ± 1.03	90.7 ± 0.65
60 hs	97.1 ± 1.21	89.7 ± 0.79
70 hs	98.6 ± 0.75	91.4 ± 0.85
80 hs	96.7 ± 1.05	89.7 ± 1.7
90 hs	95.4 ± 0.85	89.9 ± 0.52

These findings are corroborated by the image analysis results. Figures 7 and 8 displays the optical microscope images that were utilized to assess the relative densities of the hatch spacing samples manufactured with the 100 W-600 mm/s and 100 W-800 mm/s parameters. Figure 9 displays the relative densities' graphical spread. The relative densities of the samples produced with different hatch spacings are displayed numerically in Table V. It is evident from looking at Figs. 7 and 8 that the samples manufactured with a scanning speed of 800 mm/s have cavities in the structure due to high heat input. The samples produced with a scanning speed of 600 mm/s have the highest relative density, according to Table V. The sample with the highest relative density among those produced was the one produced at 600 mm/s and 70 pct hatch spacing.

Surface roughness is significantly impacted by hatch spacing changes.[24,25] Measurements of surface roughness were carried out on the top faces of the fabricated prismatic samples. Figure 10 shows a graph of surface roughness. Compared to samples manufactured with a scanning speed of 600 mm/s, those produced with a scanning speed of 800 mm/s have higher roughness values. The sample manufactured with a scanning speed

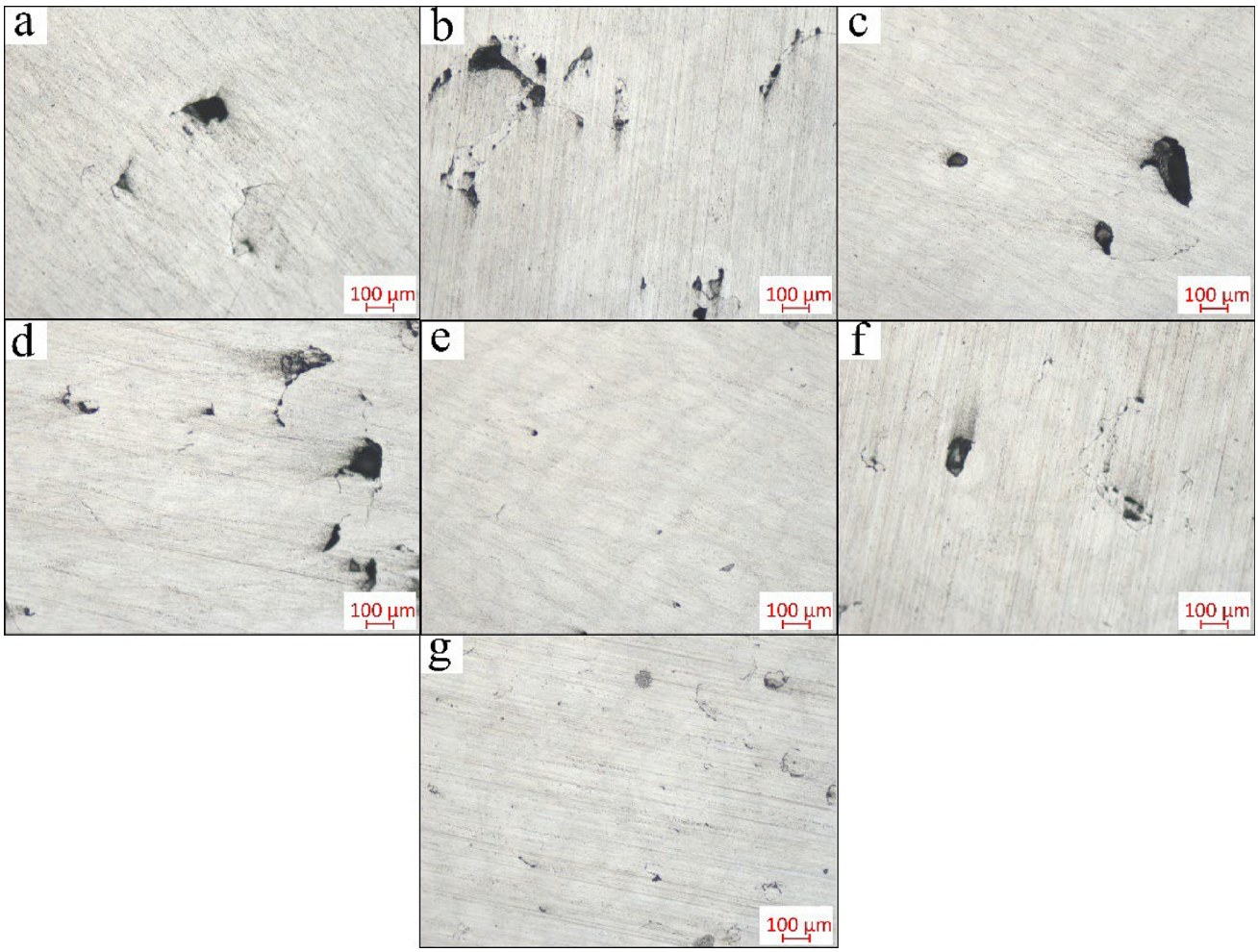

Fig. 7—Optical microscope images of prismatic samples manufactured with various hatch spacing values at 100 W-600 mm/s, (*a*) 30 pct hs, (*b*) 40 pct hs, (*c*) 50 pct hs, (*d*) 60 pct hs, (*e*) 70 pct hs, (*f*) 80 pct hs and (*g*) 90 pct hs.

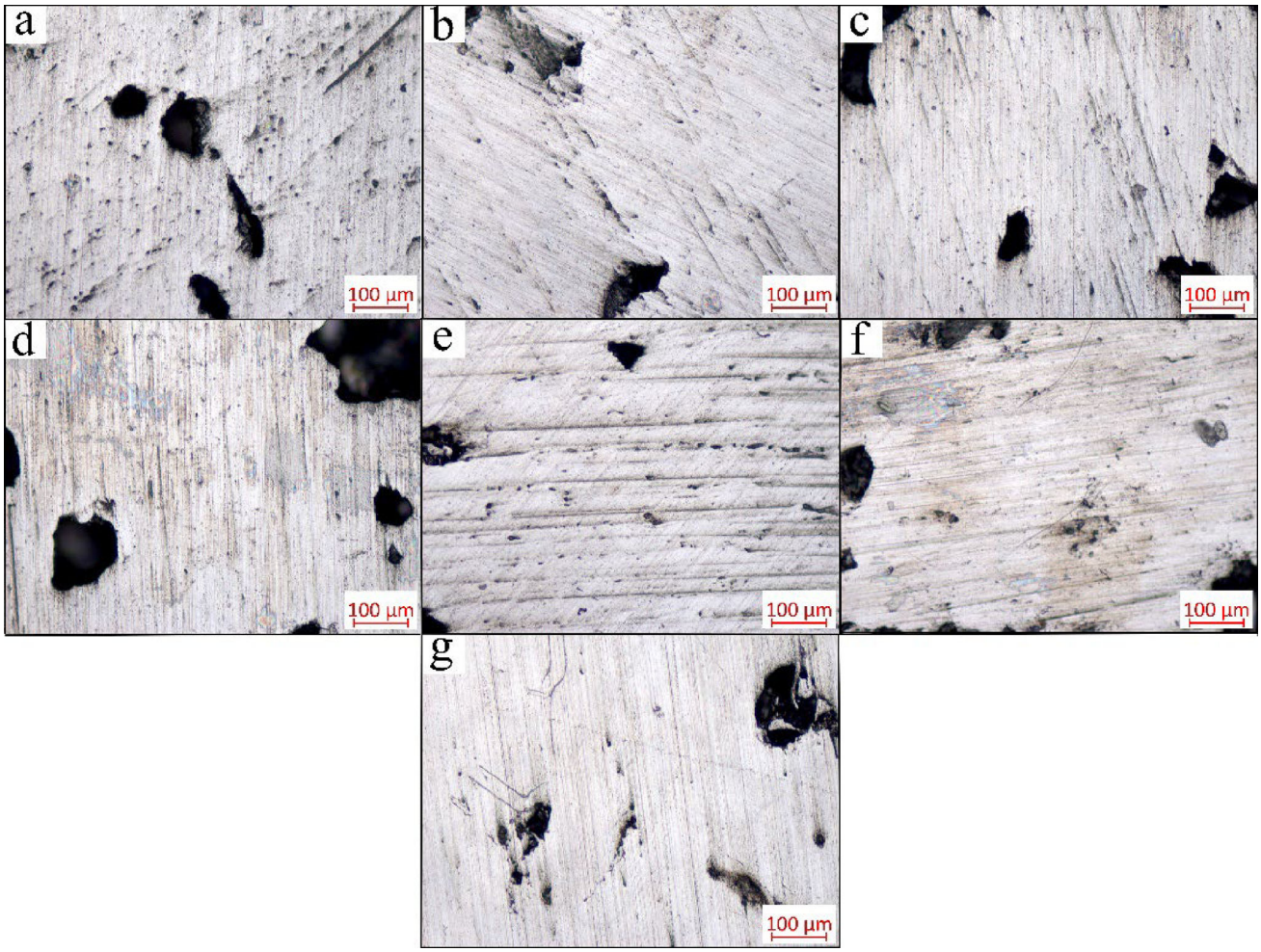

Fig. 8—Optical microscope images of prismatic samples manufactured with different hatch spacing values at 100 W-800 mm/s, (*a*) pct 30 hs, (*b*) pct 40 hs, (*c*) pct 50 hs, (*d*) pct 60 hs, (*e*) pct 70 hs, (*f*) pct 80 hs, (*g*) pct 90 hs.

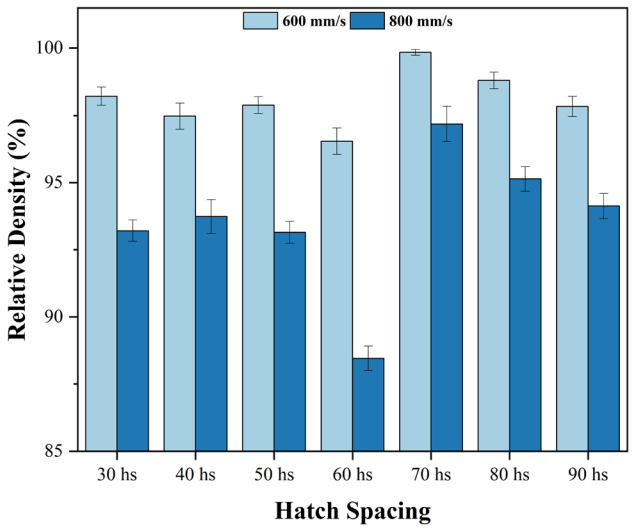

Fig. 9—Graphical distribution of relative density values determined by image analysis method.

of 600 mm/s and a hatch spacing of 70 pct had the lowest roughness value of all the samples. Additionally, this correlated with the relative density. As a result, 600 mm/s was identified as the optimum scanning speed at this point, where the highest relative density and the lowest surface roughness were achieved, and the tribological characteristics for different hatch spacing samples were investigated.

Figure 11 shows the average coefficient of friction (COF) graph for prismatic samples product with AlSi7Mg powder at different hatch spacings. It is clear from looking at the graph that all samples' COF values increased at the start of the wear test at the first contact. Later on in the test, as the surfaces adjusted to one another, the values stabilized. In Table VI, the samples' COF values are displayed. The samples manufactured with 70 and 50 pct hs values had the lowest COF values.

Figure 12 displays the wear rate and microhardness graph of the samples produced with AlSi7Mg powder. The wear graph revealed that samples manufactured at 70 pct hs had the lowest wear rate, while those

Table V. Values of Relative Densities Calculated by the Image Analysis Method

Hatch Spacing (Pct)	Relative Density (Pct)	
	100 W-600 mm/s	100 W-800 mm/s
30 hs	98.22 ± 0.39	93.21 ± 0.7
40 hs	97.48 ± 0.5	93.74 ± 1.08
50 hs	97.89 ± 0.19	93.15 ± 0.72
60 hs	96.55 ± 0.5	88.46 ± 0.79
70 hs	99.84 ± 0.05	97.19 ± 0.65
80 hs	98.80 ± 0.36	95.14 ± 0.79
90 hs	97.84 ± 0.27	94.13 ± 0.81

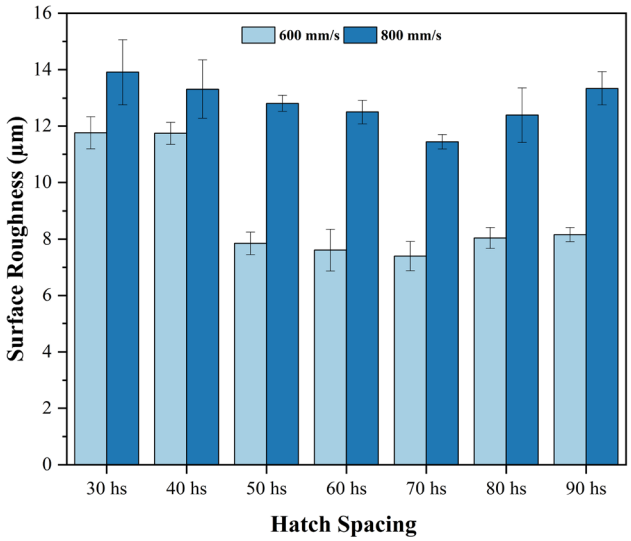

Fig. 10—Surface roughness values for prismatic samples produced using LPBF.

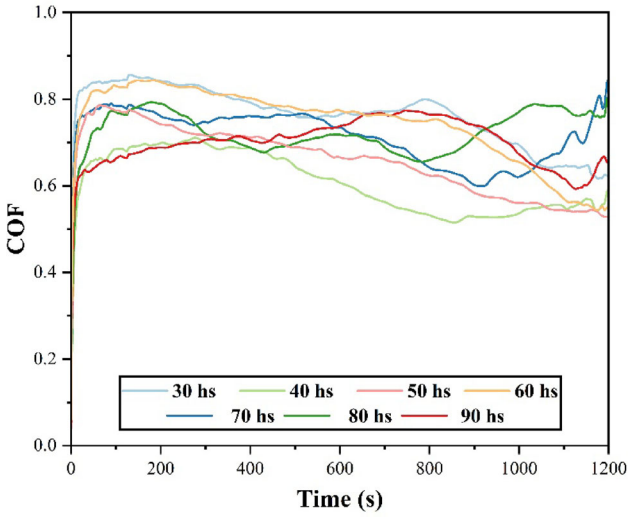

Fig. 11—COF graph for prismatic samples produced with LPBF.

manufactured at 90 pct hs had the highest wear rate. The sample with the highest relative density, 70 pct hs, was found to have the lowest wear rate. This outcome

Table VI. Values of the Average Friction Coefficient for Samples Produced Using LPBF at Different Hatch Spacings

Hatch Spacing (Pct)	COF
30	0.76 ± 0.09
40	0.71 ± 0.09
50	0.61 ± 0.08
60	0.72 ± 0.08
70	0.68 ± 0.17
80	0.70 ± 0.07
90	0.74 ± 0.1

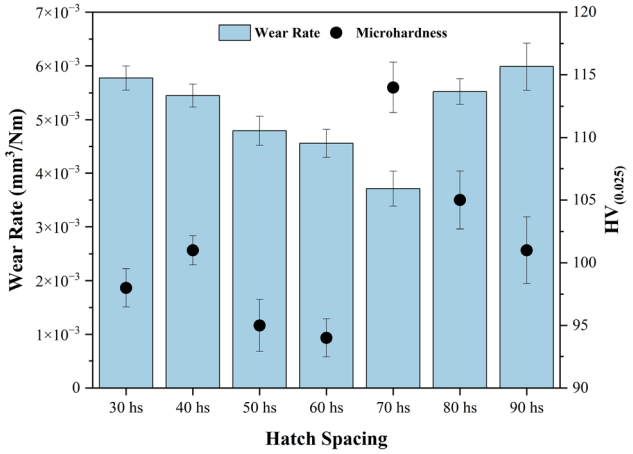

Fig. 12—Wear rates and microhardness values for prismatic samples produced with LPBF.

confirmed that maintaining the coherence of the produced item throughout the wear test and friction performance greatly depends on the relative density value. The influence of internal defects such as pores and microcracks on tribological performance must be considered. Local porosity can act as stress concentrators and promote material pull-out or crack initiation during sliding, accelerating wear. Subsurface pores lead to local contact pressure variations, inducing fluctuations in friction. In fact, Di Egidio *et al.*[26] observed that microstructural inhomogeneity and porosity influence wear behavior in LPBF AlSi10Mg under dry sliding. Similarly, Wu *et al.*[27] showed that melting mode–induced microstructural defects affect tribological properties in LPBF AlSi10Mg. Microhardness distributions revealed the sample with the highest hardness at 70 pct hs value. The sample with a 60 pct hs value exhibited the lowest hardness. The hardness of prismatic samples produced from AlSi7Mg powder material ranged from 94 ± 2.65 $HV_{0.025}$ to 114 ± 3.61 $HV_{0.025}$.

Figures 13 and 14 displays SEM and 3D-profilometer pictures of the wear traces of prismatic samples manufactured from different hatch spacing values, respectively. The samples' worn surfaces display the characteristic morphologies of abrasive wear, such as long and, distinct grooves. When compared to samples produced with various hatch spacing values, those produced with a 70 pct hs showed reduced wear trace

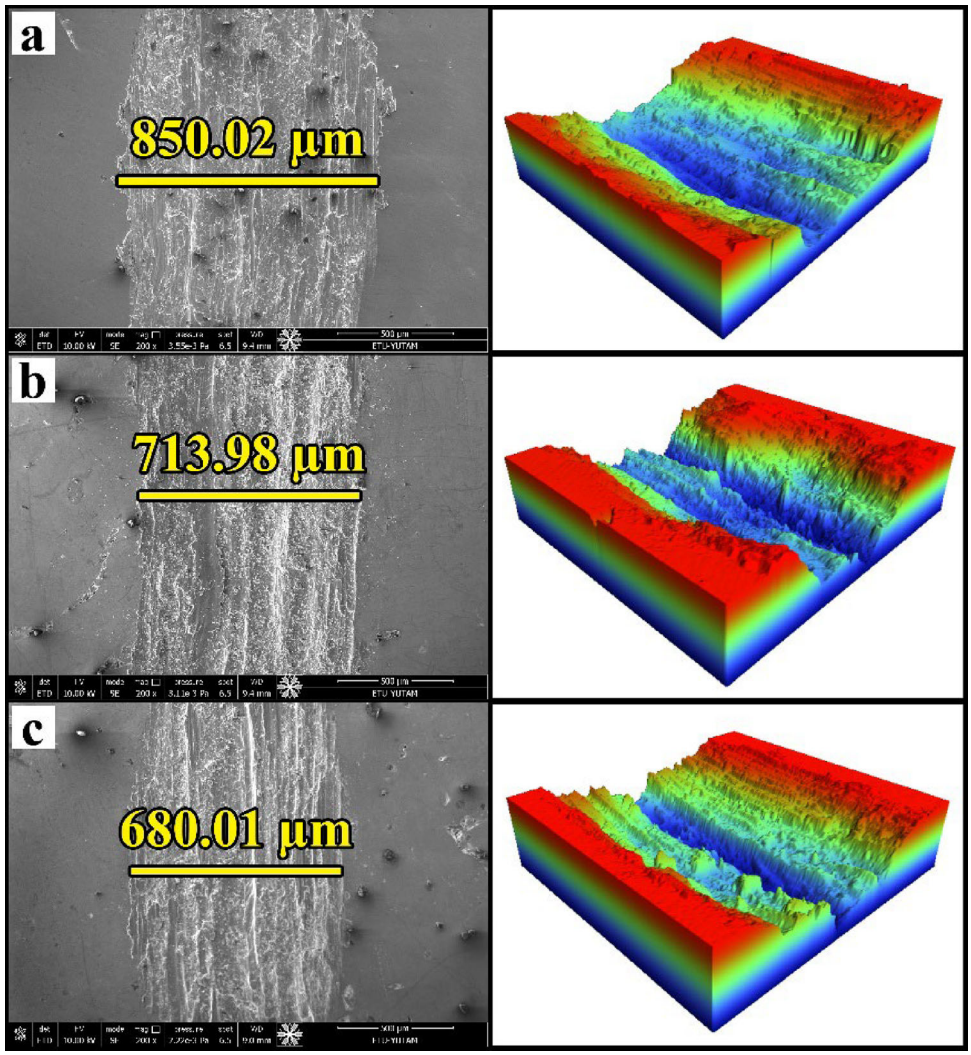

Fig. 13—Wear trace SEM and 3D profilometer images of samples manufactured using LPBF: (*a*) 30 hs, (*b*) 40 hs and (*c*) 50 hs.

depth and width. The wear behavior is significantly influenced by the nano-scale cellular Si network, which may reduce metal adhesion and prevent the development of a delamination layer.[28]

Based on the comprehensive experimental results—including microstructural analysis, density measurements, tribological and mechanical performance evaluations—the optimal LPBF process parameters for AlSi7Mg alloy production have been determined and are presented in Table VII.

B. *Optimizing of Construction Angle in LPBF*

Prismatic AlSi7Mg samples were fabricated at three distinct angles (0, 45, and 90 deg) using the processing parameters listed in Table VII to identify the optimal construction angle. The density values measured by the Archimedes method ranged from 2.56 to 2.64 g/cm^3. These results confirm that the LPBF process parameters used in this study produced structurally dense components, as the obtained values are comparable to the theoretical density of cast AlSi7Mg 2.68 g/cm in the literature.[29] This finding further supports the microstructural observations from optical microscopy, which revealed minimal porosity in the optimally processed samples. Figure 15 depict the optical micrographs of AlSi7Mg samples fabricated at build orientations of 0, 45, and 90 deg, respectively. These images primarily reveal the general surface texture, porosity distribution, and relative density of the samples prior to chemical etching. In the 0 deg sample [Figure 15(a)], the microstructure appears relatively uniform with minimal dark regions, indicating a low level of porosity and a dense, well-fused structure. The absence of large voids or defects suggests efficient laser energy absorption and melt pool consolidation during the additive manufacturing process. In contrast, the 45 deg sample [Figure 15(b)] exhibits a noticeable presence of irregular dark spots, likely corresponding to lack-of-fusion defects or trapped gas pores. These defects appear more clustered, potentially due to suboptimal melt overlap or scan strategy inconsistencies at this intermediate orientation. The sample of 90 deg [Figure 15(c)] shows a more homogenous surface with finely dispersed dark

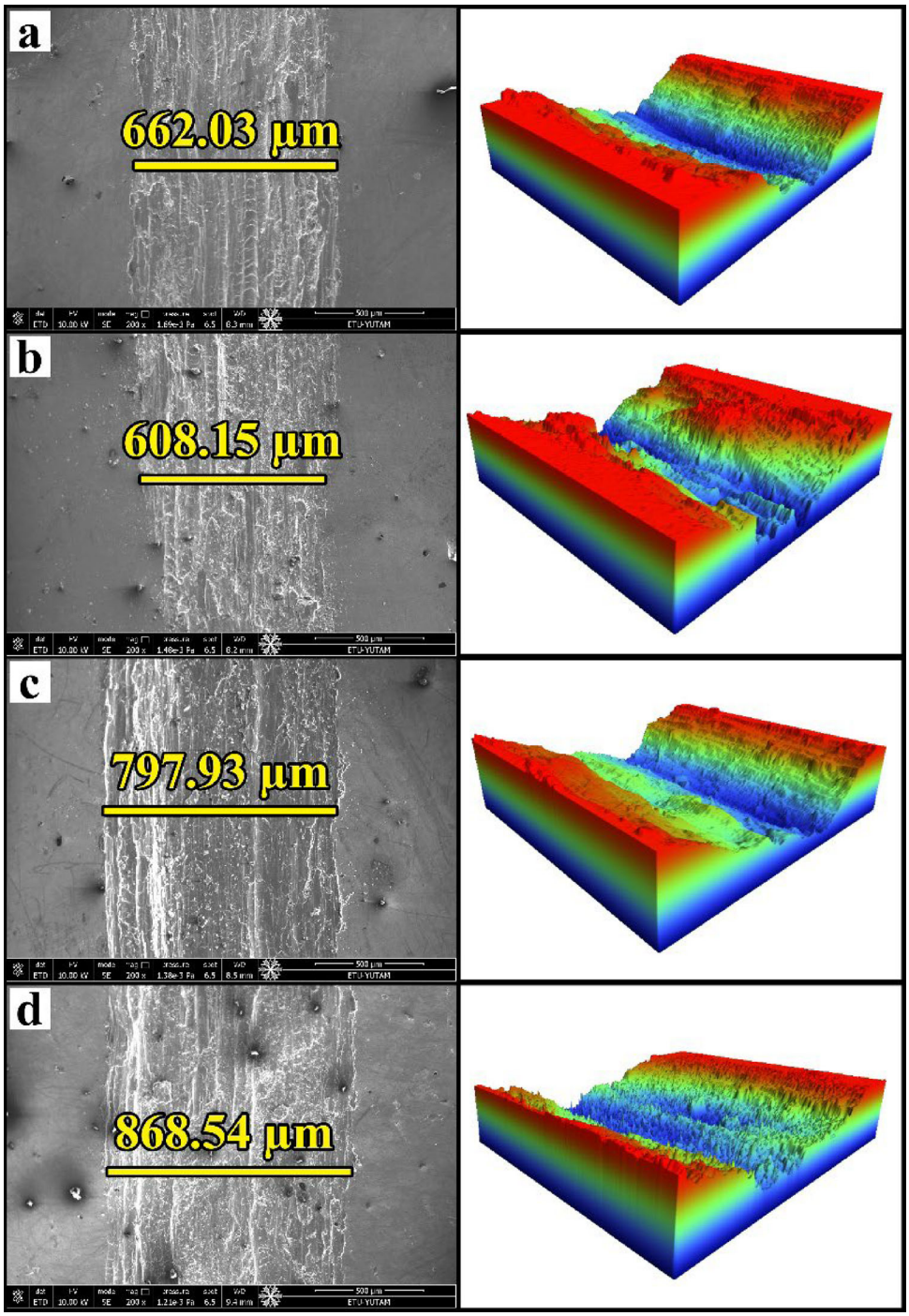

Fig. 14—Wear trace SEM and 3D profilometer images of samples manufactured using LPBF: (*a*) 60 hs, (*b*) 70 hs, (*c*) 80 hs and (*d*) 90 hs.

Table VII. Optimal LPBF Parameter Configuration for AlSi7Mg Alloy

Laser Power (W)	Scanning Speed (mm/s)	Layer Thickness (μm)	Hatch Spacing (pct)
100	600	15	70

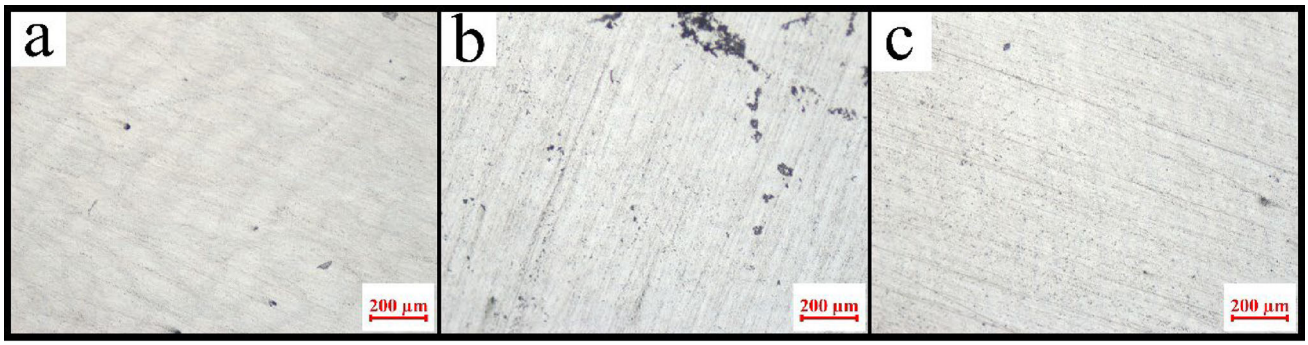

Fig. 15—Optical microscope image of AlSi7Mg samples produced at different construction angles: (*a*) 0 deg, (*b*) 45 deg and (*c*) 90 deg.

features, indicative of uniformly distributed micro--pores. Overall, the optical observations suggest that the 0 deg orientation results in the highest apparent density, while the sample of 45 deg presents the most visible porosity. The sample of 90 deg lies between these two extremes, with relatively better fusion than the sample of 45 deg but not as dense as the sample of 0 deg.

The relative density values of these samples, as determined by both the Archimedes method and image analysis, are displayed in Table VIII. It can be observed that the sample produced with a 0 deg construction angle has the highest relative density value.

Figure 16 present the optical micrographs of AlSi7Mg alloy samples fabricated at 0, 45, and 90 deg build orientations, in turn. Following the fabrication process, all samples were etched with Keller's reagent to reveal the underlying microstructural properties. In the sample built at 0 deg [Figure 16(a)], a well-aligned and relatively uniform cellular structure is observed, with melt pool boundaries running parallel to the build direction. This indicates a strong directional solidification influenced by the thermal gradient aligned with the laser scanning path. The 45 deg oriented sample [Figure 16(b)] exhibits a more complex and interwoven cellular pattern, suggesting multidirectional heat flow and more irregular solidification fronts. The melt pool boundaries appear less uniform, and the cellular features are denser and more entangled. In contrast, the sample of 90 deg [Figure 16(c)] reveals a distinct layered structure with prominently visible melt pool lines oriented perpendicular to the build direction. The cellular features are more elongated and aligned with the deposition layers, reflecting the influence of layer-by-layer thermal cycles.

To investigate the microstructural characteristics and phases of AlSi7Mg alloy, prismatic samples were fabricated using optimal manufacturing parameters, and SEM analysis was performed on their surfaces, as shown in Figure 17. The SEM images reveal three distinct microstructural regions across all build orientations (0, 45, and 90 deg): the fine zone, coarse zone, and heat-affected zone (HAZ). These zones arise due to thermal gradients and variations in solidification rates during the LPBF process. The cooling rate, which is a function of both the temperature gradient and solidification velocity, plays a critical role in determining microstructure scale. Higher cooling rates lead to greater undercooling and thus promote the formation of finer microstructures. The spatial variation in cooling rate arises from the Gaussian intensity profile of the laser beam, with the highest cooling occurring at the melt pool center and progressively reducing toward the edges. Consequently, grains in the center are finer (fine zone), while coarser grains form at the periphery (coarse zone). The HAZ is located adjacent to the melt pool, in the overlap region with previous scan tracks, where residual heat can induce grain coarsening and localized Si precipitation. In the 0 deg build orientation, the melt pools are oriented horizontally, showing symmetric and layered structures with well-defined fine and coarse zones. The 45 deg orientation results in diagonal melt pools with more irregular zone boundaries, while the 90 deg orientation exhibits curved and vertically stacked melt pools with thicker and more continuous HAZs. High-magnification SEM images further reveal the evolution of the Si network within the Al matrix, which is strongly influenced by the build orientation and associated thermal history. In all samples, a portion of the Si atoms dissolves directly into the Al matrix, while the remaining Si rapidly precipitates to form an interconnected or fragmented network along grain and subgrain boundaries, depending on local cooling conditions. This behavior contrasts with the continuous Al-Si eutectic typically observed in cast structures and is consistent with findings reported in prior LPBF studies.[9,30–34] Overall, the observed variations in microstructure and Si distribution are closely related to differences in heat flow and solidification dynamics governed by the build orientation.

Figure 18 shows the XRD results for samples produced with different construction angles using AlSi7Mg powder and LPBF process. The powder sample exhibits characteristic diffraction peaks corresponding to the face-centered cubic (FCC) structure of aluminum, including Al (111), Al (200), Al (220), and Al (311) planes. The relative intensities of these peaks suggest a randomly oriented, polycrystalline microstructure, typical of atomized metal powders.

In contrast, the XRD pattern of the LPBF-fabricated bulk sample reveals distinct differences in peak intensities, indicating the presence of crystallographic texture induced by the rapid solidification and directional thermal gradients inherent to the LPBF process.

Table VIII. Relative densities of samples produced using various construction angles

Construction Angles (Deg)	Relative Density (Pct) Archimedes' Method	Relative Density (Pct) Image Analysis Method
0	98.6 ± 0.75	99.84 ± 0.05
45	96.2 ± 0.52	96.98 ± 1.3
90	95.5 ± 0.88	99.71 ± 0.1



Fig. 16—Optical microscope image of AlSi7Mg samples produced at different construction angles: (*a*) 0 deg, (*b*) 45 deg and (*c*) 90 deg.

Notably, the Al (111) and Al (200) peaks exhibit enhanced intensities, suggesting preferred grain orientations along these planes. Furthermore, the emergence of additional peaks corresponding to Si (111) and Mg_2Si (311) planes indicates the formation of secondary phases during the solidification process. The presence of the Mg_2Si phase, in particular, is attributed to elemental segregation and precipitation during rapid solidification, contributing to the age-hardening response of the alloy. Crystallographic texture in LPBF-manufactured parts is known to be highly sensitive to the build orientation. According to existing literature, different construction angles (0, 45, and 90 deg relative to the build plate) significantly influence the solidification direction and resulting grain orientation: 0 deg build orientation typically leads to upward solidification along the build direction, favoring strong Al (111) texture due to its low surface energy. 45 deg orientation induces a more complex thermal gradient, resulting in more evenly distributed intensities among Al (111), Al (200), and Al (220) planes. In contrast, the intensity of the peak belonging to the Al (200) plane in the 90 deg orientation is significantly lower than in the 0 and 45 deg orientations. This indicates that the crystal structure in the sample produced in the 90 deg orientation is less aligned along the Al (200) plane, while there is more orientation toward the (111) and (220) planes. Therefore, it can be said that the crystallographic texture in this sample develops predominantly along the (111) and (220) planes[35,36] . The observed variations in peak intensities between the powder and bulk samples confirm that the LPBF process significantly alters the microstructure of the alloy, introducing crystallographic texture and promoting the formation of intermetallic phases. These microstructural evolutions have critical implications for the mechanical performance of the final component, particularly in terms of tensile strength, ductility, and fatigue resistance. In addition to the microstructural observations above, the crystallographic texture developed during LPBF is also expected to influence tribological responses. Preferred orientations such as (111) and (220), which possess higher atomic-packing density, may enhance resistance to shear deformation and local plastic strain during sliding, thereby contributing to improved wear stability.[37]

Figure 19 shows the COF graph derived for the samples. The friction coefficient curves for all samples were extremely similar. The sample with a construction angle of 45 deg had the lowest COF value.

Figure 20 shows the wear rate and microhardness graphs for samples produced with different construction angles. The figure indicates that the sample produced at a 90 deg angle has the minimum hardness, while the maximum hardness is recorded in the 0 deg oriented sample. For 0 deg build orientation, the average hardness values were 114 ± 3.61 $HV_{0.025}$; for 45 deg build orientation, they were 100.5 ± 1.32 $HV_{0.025}$; and for 90 deg construction angle, they were 96.8 ± 0.91 $HV_{0.025}$. Similar investigations to microhardness values were identified in the literature, and the findings were determined to be coherent.[38,39] The variation in microhardness values is directly governed by the cellular microstructure refinement characteristic of the LPBF process. The rapid solidification produces a fine cellular Al structure with Si-rich boundaries, creating a composite-like strengthening effect.[36] The highest hardness (114 HV ± 3.61) is achieved in samples with the optimal melt pool morphology and overlap (0 deg orientation, 70 pct hatch spacing), which promote the formation of a finer and more uniform cellular network. This enhances grain boundary strengthening and solid solution hardening.[40] In contrast, samples with non-optimal

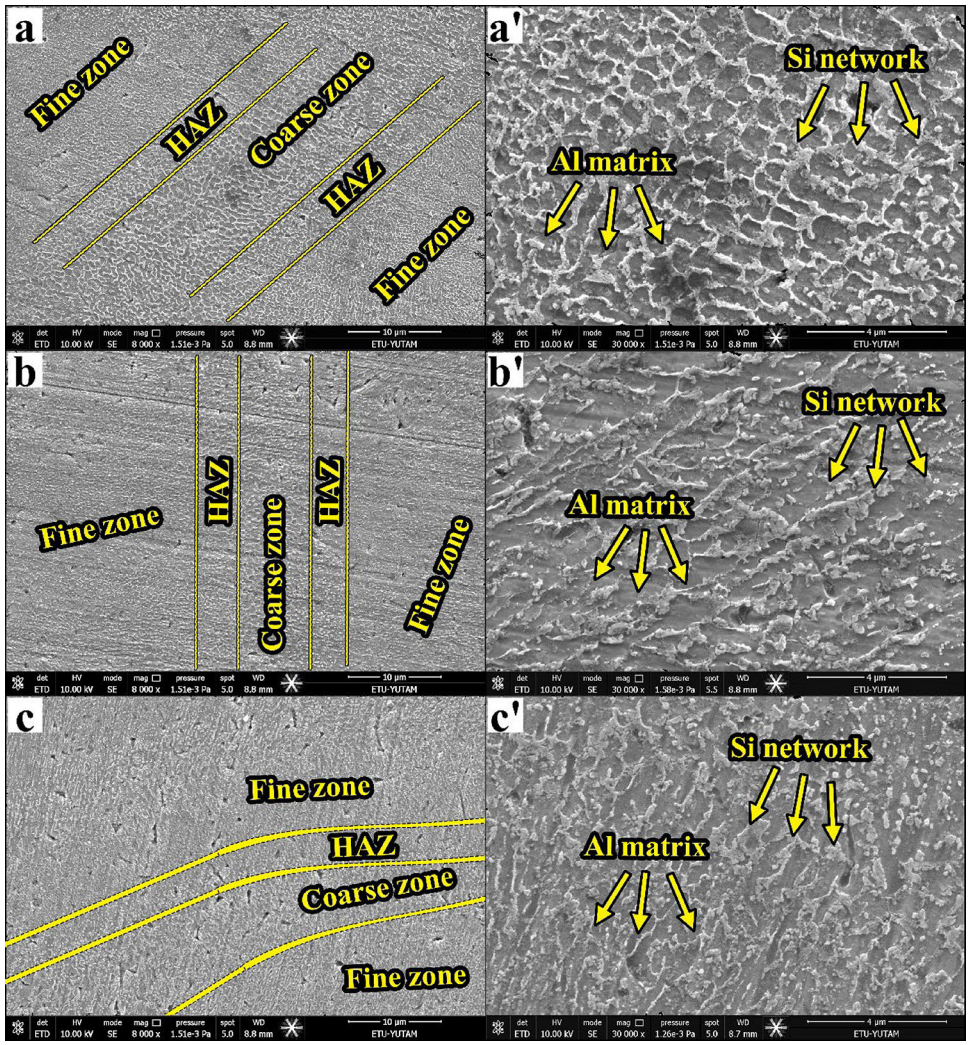

Fig. 17—Microstructure SEM images of AlSi7Mg samples manufactured at various construction angles (*a*)–(*a*)′ 0 deg, (*b*)–(*b*)′ 45 deg and (*c*)–(*c*)′ 90 deg.

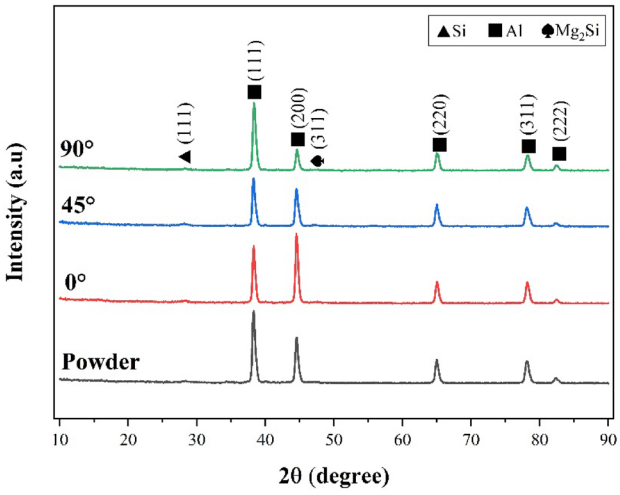

Fig. 18—XRD graph of powder and AlSi7Mg samples manufactured at various construction angles.

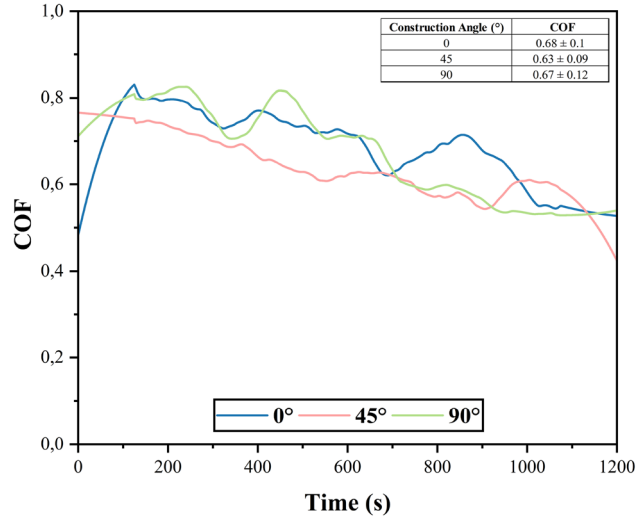

Fig. 19—COF graphs of samples manufactured at different construction angles using LPBF.

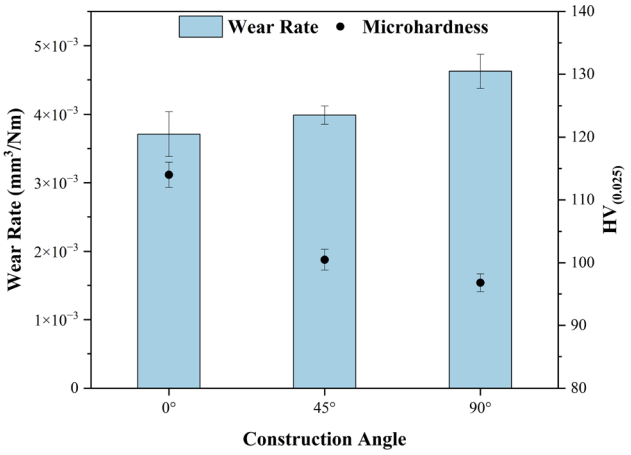

Fig. 20—The microhardness graph and wear rate of the samples produced with different construction angles.

parameters exhibit coarser microstructures and potential defects, leading to reduced hardness.[41] When the wear and microhardness graphs were studied jointly, it appeared that the wear rate was oppositely proportional to hardness. Wear rates were lowest in the sample manufactured with a 0 deg construction angle and highest in the sample manufactured with a 90 deg construction angle. The observed inverse relationship between the COF and wear rate across different build orientations can be attributed to a shift in the dominant wear mechanism. The 45 deg sample, with its intermediate density and hardness, undergoes localized delamination due to stress concentration at porosity sites. The generated wear debris acts as third-body particles at the interface. It is well-established that such debris can roll or slide, reducing the shear stress and thus the COF, while simultaneously accelerating material removal and leading to a high wear rate.[42,43] In contrast, the 90 deg sample, with the lowest hardness, is most susceptible to direct abrasive penetration, resulting in the highest wear rate through a classical abrasive wear mechanism. The 0 deg orientation, with its optimal combination of high density and hardness, effectively resists both mechanisms, yielding the lowest wear rate.

Figure 21 presents SEM micrographs of wear traces and optical profilometer images for samples fabricated at three distinct build orientations (0, 45, 90 deg) using the optimized LPBF parameters. Comparative analysis revealed that the 0 deg orientation exhibited the narrowest and shallowest wear trace, while increasing construction angles correlated with progressive widening of wear traces. This trend is attributed to residue accumulation during testing, which promotes non-uniform wear through surface cracking, adhesive transfer, or particle ejection.[44] The relatively smooth and shallow grooves observed for the 0 deg samples indicate a predominantly mild abrasive wear mechanism, consistent with their higher hardness and density. In contrast, the 45 and 90 deg samples displayed evidence of severe material removal, delamination, and transfer-layer formation, suggesting a mixed adhesive–abrasive wear mechanism. Similar morphological transitions with build orientation have been reported in LPBF Al–Si–Mg alloys under dry sliding conditions.[27,45]

The sample with 0 deg construction angle showed better results in all tests except COF values when microhardness, wear rate and microstructures were evaluated collectively. It was found that the sample with a construction angle of 0 deg and the sample with a construction angle of 90 deg had extremely similar COF values. Furthermore, the sample with a 90 deg construction angle took nearly twice as long to manufacture as the sample with a 0 deg construction angle, which would raise expenses. For these reasons, the ideal construction angle was found to be 0 deg. The texture effect, combined with the fine cellular microstructure and the more uniform Si network, supports the superior wear performance observed for the 0 deg build orientation, where directional heat flow promotes stronger alignment of grain growth. This observation aligns with recent findings on the effect of build orientation on microstructure development in LPBF-processed alloys.[46]

V. CONCLUSIONS

This study comprehensively investigated the influence of critical LPBF process parameters—namely laser power, scanning speed, hatch spacing, and build orientation—on the structural, mechanical, and tribological properties of AlSi7Mg alloy fabricated via LPBF.

- Through systematic optimization of process conditions, the optimal parameter combination was determined to be 100 W laser power, 600 mm/s scanning speed, 15 μm layer thickness, and 70 pct hatch spacing. These parameters yielded a relative density of approximately 99 pct and a peak microhardness value of 114 ± 3.61 $HV_{0.025}$.
- Wear and friction analyses revealed that the 0 deg build orientation provided superior tribological performance, exhibiting the lowest wear rate and the narrowest wear traces, while the 90 deg orientation showed increased wear due to less favorable surface integrity.
- Microstructural investigations using SEM confirmed the formation of distinct melt pool geometries and cellular microstructures depending on build orientation, driven by the directional nature of heat flow and solidification during LPBF.
- XRD analyses supported these findings by revealing the development of crystallographic texture and the formation of Si and intermetallic phases such as Mg_2Si in the LPBF-fabricated samples—features absent or less prominent in the feedstock powder.
- The 0 deg build orientation was identified as the most favorable, not only for its superior mechanical and tribological performance, but also due to its reduced build time and manufacturing efficiency.

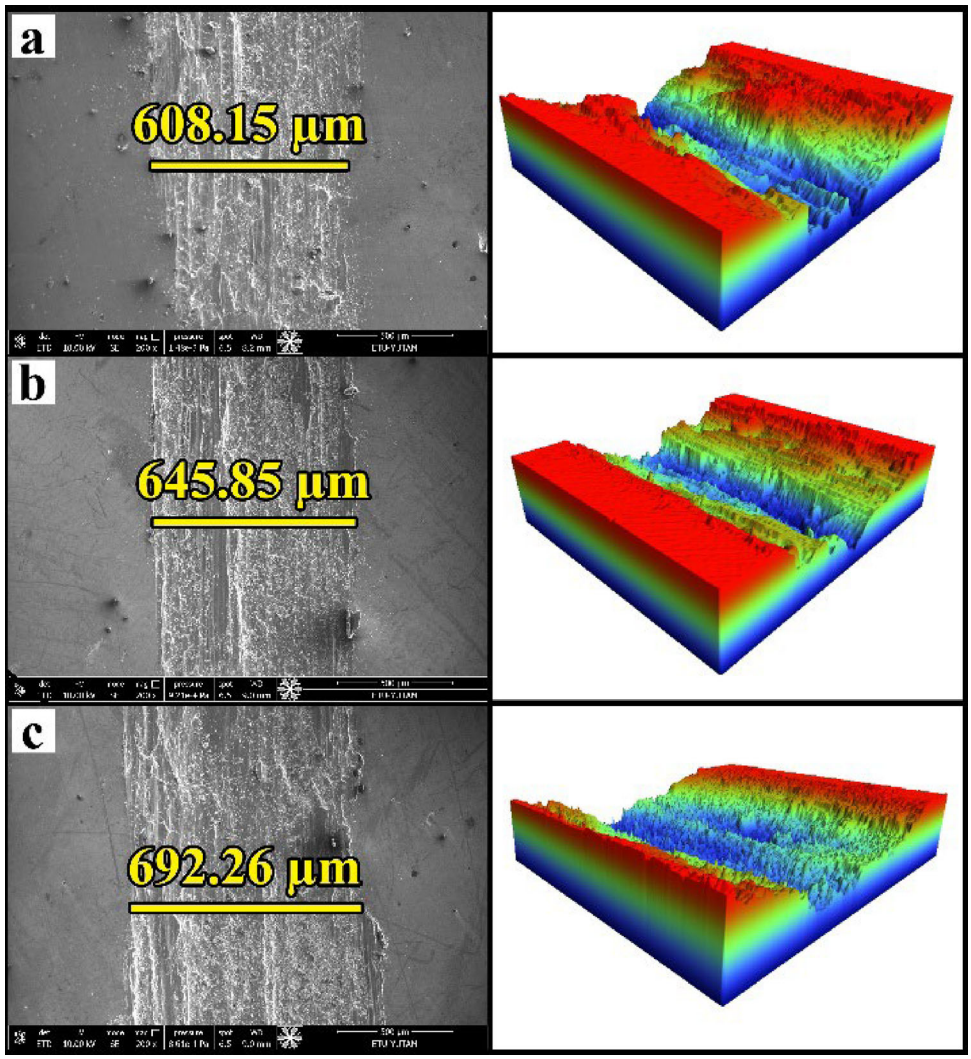

Fig. 21—SEM and 3D-profilometer images of the wear traces of AlSi7Mg samples produced at various construction angles: (*a*) 0 deg, (*b*) 45 deg and (*c*) 90 deg.

Collectively, the findings emphasize the critical role of hatch spacing and build orientation—factors often overlooked in prior studies—in governing the final properties of AlSi7Mg components. These insights contribute to the ongoing development of high-performance aluminum alloys for additive manufacturing, particularly where wear resistance and structural integrity are of paramount importance.

However, this study did not investigate the effects of post-processing techniques such as heat treatment and surface treatments on LPBF-produced parts. As a result, it is advised that future research concentrate on the implications of post-processing and dynamic mechanical qualities.

ACKNOWLEDGMENTS

We thank Erzurum Technical University High Technology Research and Application Center (ETÜ-YÜTAM) for its support in experimental studies, and the Higher Education Council of Türkiye (YÖK) for providing scholarships to Furkan CENGİZ within the scope of the 100/2000 program.

AUTHOR CONTRIBUTIONS

Furkan Cengiz: investigation, writing—review and editing, validation. Tevfik Oğuzhan Ergüder: investigation, writing—review and editing, validation. Fatih Yıldız: conceptualization, writing—review and editing, supervision.

FUNDING

No funding was received for conducting this study.

DATA AVAILABILITY

The raw and processed data generated during this study will be made available upon reasonable request.

CONFLICT OF INTEREST

The authors declare that they have no known competing financial interests or personal relationships that could have appeared to influence the work reported in this paper.

REFERENCES

1. O.O. Joseph, P.A. Olubambi, O.O. Joseph, B.M. Edun, J.O. Okeniyi, and O.P. Abioye: *IOP Conf. Ser. Mater. Sci. Eng.*, 2021, vol. 1107, p. 012116.
2. L. Thijs, K. Kempen, J.-P. Kruth, and J. Van Humbeeck: *Acta Mater.*, 2013, vol. 61, pp. 1809–19.
3. T. Zou, S. Mei, M. Chen, and H. Zhu: *J. Mater. Eng. Perform.*, 2023, vol. 32, pp. 296–304.
4. X. Li, L. Zhang, and X. Wei: *J. Mater. Sci.*, 2024, vol. 59, pp. 258–76.
5. A.B. Spierings, K. Dawson, K. Kern, F. Palm, and K. Wegener: *Mater. Sci. Eng. A*, 2017, vol. 701, pp. 264–73.
6. D. Koutny, D. Skulina, L. Pantělejev, D. Paloušek, B. Lenczowski, F. Palm, and A. Nick: *Procedia CIRP*, 2018, vol. 74, pp. 44–48.
7. J. Wang, B. He, C. Liu, L. Lan, S. Gao, and Y. Rong: *Met. Mater. Int.*, 2024, vol. 30, pp. 2882–97.
8. X. Ni, Y. Liang, Z. Hu, W. Yang, A. Wang, X. Deng, H. Wang, S. Wu, and G. Nie: *Metall. Mater. Trans. B*, 2025, vol. 56B, pp. 2137–43.
9. H. Rao, S. Giet, K. Yang, X. Wu, and C.H.J. Davies: *Mater. Des.*, 2016, vol. 109, pp. 334–46.
10. Q. Yang, C. Xia, Y. Deng, X. Li, and H. Wang: *Materials*, 2022, https://doi.org/10.3390/ma12162525.
11. T. Kimura and T. Nakamoto: *Mater. Des.*, 2016, vol. 89, pp. 1294–1301.
12. L. Tonelli, E. Liverani, A. Morri, and L. Ceschini: *Metall. Mater. Trans. B*, 2021, vol. 52B, pp. 2484–96.
13. R. Casati and M. Vedani: *Adv Eng Mater*, https://doi.org/10.1002/adem.201800406.
14. J.C. Pereira, E. Gil, L. Solaberrieta, M. San Sebastián, Y. Bilbao, and P.P. Rodríguez: *Materials Science and Engineering: A*, https://doi.org/10.1016/j.msea.2020.139124.
15. J.T. Oliveira de Menezes, E.M. Castrodeza, and R. Casati: *Materials Science and Engineering: A*, https://doi.org/10.1016/j.msea.2019.138392.
16. M. Tang and P.C. Pistorius: *Int. J. Fatigue*, 2017, vol. 94, pp. 192–201.
17. K.V. Yang, P. Rometsch, T. Jarvis, J. Rao, S. Cao, C. Davies, and X. Wu: *Mater. Sci. Eng. A*, 2018, vol. 712, pp. 166–74.
18. M. Wang, Y. Zhang, B. Song, Q. Wei, and Y. Shi: *Acta Metall. Sin. (English Lett.)*, 2021, vol. 34, pp. 1213–22.
19. S. Venettacci, G.S. Ponticelli, D. Guarino, and S. Guarino: *J. Manuf. Process.*, 2022, vol. 84, pp. 1103–21.
20. E. Li, Z. Zhou, L. Wang, R. Zou, and A. Yu: *Powder Technol.*, 2022, vol. 400, p. 117262.
21. T. Qi, H. Zhu, H. Zhang, J. Yin, L. Ke, and X. Zeng: *Mater. Des.*, 2017, vol. 135, pp. 257–66.
22. N.T. Aboulkhair, I. Maskery, C. Tuck, I. Ashcroft, and N.M. Everitt: *J. Mater. Process. Technol.*, 2016, vol. 230, pp. 88–98.
23. J.P. Kruth, L. Froyen, J. Van Vaerenbergh, P. Mercelis, M. Rombouts, and B. Lauwers: *J. Mater. Process. Technol.*, 2004, vol. 149, pp. 616–22.
24. B. Whip, L. Sheridan, and J. Gockel: *Int. J. Adv. Manuf. Technol.*, 2019, vol. 103, pp. 4411–22.
25. J.C. Fox, S.P. Moylan, and B.M. Lane: *Procedia CIRP*, 2016, vol. 45, pp. 131–34.
26. G. Di Egidio, C. Martini, J. Börjesson, E. Ghassemali, L. Ceschini, and A. Morri: *Wear*, 2023, vol. 516–517, p. 204602.
27. H. Wu, Y. Ren, J. Ren, A. Cai, M. Song, Y. Liu, X. Wu, Q. Li, W. Huang, X. Wang, and I. Baker: *Virtual Phys. Prototype*, 2020, vol. 15, pp. 570–82.
28. K.G. Prashanth, B. Debalina, Z. Wang, P.F. Gostin, A. Gebert, M. Calin, U. Kühn, M. Kamaraj, S. Scudino, and J. Eckert: *J. Mater. Res.*, 2014, vol. 89, pp. 2044–54.
29. S. Vaudreuil, S.E. Bencaid, H.R. Vanaei, and A. El Magri: *Materials*, 2022, https://doi.org/10.3390/ma15238640.
30. X. Wang, L.Q. Li, J. Qu, and W. Tao: *Mater. Sci. Technol.*, 2019, vol. 35, pp. 1–10.
31. E. Cerri, E. Ghio, and G. Bolelli: *J. Mater. Eng. Perform.*, 2021, vol. 30, pp. 4981–92.
32. K.L. Fan, G.Q. He, X.S. Liu, B. Liu, M. She, Y.L. Yuan, Y. Yang, and Q. Lu: *Mater. Sci. Eng. A*, 2013, vol. 586, pp. 78–85.
33. Y. Birol: *J. Alloys Compd.*, 2007, vol. 439, pp. 81–86.
34. X. Dong, L. He, G. Mi, and P. Li: *J. Alloys Compd.*, 2015, vol. 618, pp. 609–14.
35. W.J. Hwang, G.B. Bang, and S.H. Choa: *Met. Mater. Int.*, 2023, vol. 29, pp. 1311–22.
36. M. Wang, B. Song, Q. Wei, Y. Zhang, and Y. Shi: *Mater. Sci. Eng. A*, 2019, vol. 739, pp. 463–72.
37. H. Liu, D. Gu, L. Xi, H. Zhang, K. Shi, B. Wu, R. Zhang, and J. Qi: *Addit. Manuf. Front.*, 2024, vol. 3, p. 200145.
38. T. Zou, M. Chen, H. Zhu, and S. Mei: *J. Mater. Eng. Perform.*, 2022, vol. 31, pp. 1791–1802.
39. J. Zvoníček, D. Koutný, L. Pantělejev, and D. Paloušek: in *Current Methods of Construction Design*, Š. Medvecký, S. Hrček, R. Kohár, F. Brumerčík, and V. Konstantová, eds., Springer International Publishing, Cham, 2020, pp. 515–24.
40. N.T. Aboulkhair, I. Maskery, C. Tuck, I. Ashcroft, and N.M. Everitt: *Mater. Sci. Eng., A*, 2016, vol. 667, pp. 139–46.
41. N. Takata, H. Kodaira, A. Suzuki, and M. Kobashi: *Mater. Charact.*, 2018, vol. 143, pp. 18–26.
42. J. Jiang, F.H. Stott, and M.M. Stack: *Tribol. Int.*, 1998, vol. 31, pp. 245–56.
43. K. Kato: *Wear*, 2000, vol. 241, pp. 151–57.
44. A. Igual Muñoz and S. Mischler: *J. Mater. Sci. Mater. Med.*, 2011, vol. 22, pp. 437–50.
45. P. Tonolini, L. Montesano, M. Tocci, A. Pola, and M. Gelfi: *Adv. Eng. Mater.*, 2021, https://doi.org/10.1002/adem.202100147.
46. P.V. Cobbinah, S. Matsunaga, and Y. Yamabe-Mitarai: *Adv. Eng. Mater.*, 2023, vol. 25, p. 25.

Publisher's Note Springer Nature remains neutral with regard to jurisdictional claims in published maps and institutional affiliations.

Springer Nature or its licensor (e.g. a society or other partner) holds exclusive rights to this article under a publishing agreement with the author(s) or other rightsholder(s); author self-archiving of the accepted manuscript version of this article is solely governed by the terms of such publishing agreement and applicable law.